Detectable Changes in the Frequency of Temperature Extremes

Detectable Changes in the Frequency of Temperature Extremes

SIMONE MORAK AND GABRIELE C. HEGERL

School of Geosciences, University of Edinburgh, Edinburgh, United Kingdom

NIKOLAOS CHRISTIDIS

Met Office Hadley Centre for Climate Change, Exeter, United Kingdom

(Manuscript received 21 November 2011, in final form 3 August 2012)

ABSTRACT

This study determines whether observed recent changes in the frequency of hot and cold extremes over land can be explained by climate variability or whether they show a detectable response to external influences. The authors analyze changes in the frequency of moderate-to-extreme daily temperatures—namely, the number of days exceeding the 90th percentile and the number of days not reaching the 10th percentile of daily minimum (tn90 and tn10, respectively) and maximum (tx90 and tx10, respectively) temperature—for both cold and warm seasons. The analysis is performed on a range of spatial scales and separately for boreal cold- and warm-season data. The fingerprint for external forcing is derived from an ensemble of simulations produced with the Hadley Centre Global Environmental Model, version 1 (HadGEM1), with both anthropogenic and natural forcings. The observations show an increase in warm extremes and a decrease in cold extremes in both seasons and in almost all regions that are generally well captured by the model. Some regional differences between model and observations may be due to local forcings or changes in climate dynamics. A detection analysis, using both optimized and nonoptimized fingerprints, shows that the influence of external forcing is detectable in observations for both cold and warm extremes, and cold and warm seasons, over the period 1951–2003 at the 5% level. It is also detectable separately for the Northern and Southern Hemispheres, and over most regions analyzed. The model shows a tendency to significantly overestimate changes in warm daytime extremes, particularly in summer.

1. Introduction

Studies of observational temperature records over the last 50–100 years have found evidence for an increase in both observed mean (Trenberth et al. 2007) and extreme near-surface temperatures (Frich et al. 2002; Alexander et al. 2006; Caesar et al. 2006; Brown et al. 2008). Similar changes have also been found in model simulations (Kharin and Zwiers 2000; Tebaldi et al. 2006; Kharin et al. 2007).

Studying changes in temperature extremes, as well as attributing and predicting those changes, is of great importance as extreme temperature events can seriously affect human health, ecosystems, and the economy (Solomon et al. 2007; Karl et al. 2008).

Alexander et al. (2006) show that there has been a significant increase in temperature extremes during the second half of the twentieth century, particularly in the warm tail of both minimum and maximum surface temperature distributions. However, the increase in maximum temperature has been of smaller magnitude, which has led to a decrease in the diurnal temperature range, largely caused by differential warming during the period prior to the 1980s (Vose et al. 2005; Trenberth et al. 2007). While warm extremes have been increasing, there has been a decrease in cold extremes (Alexander et al. 2006; Karl et al. 2008).

Besides these global trends in temperature extremes, there have also been noticeable changes on regional scales, such as a strong decrease in the number of frost days and an increase in season length across northwestern North America and eastern Europe. An increase in the number of heat waves has also been observed in southwestern North America (Tebaldi et al. 2006). In contrast to the observed increase in warm extremes, Portmann et al. (2009) found the change in the number of hot daytime extremes across eastern North America to be modest, with decreases over the southeastern part

Corresponding author address: Simone Morak, School of Geosciences, University of Edinburgh, West Mains Road, Edinburgh EH9 3JW, United Kingdom.
E-mail: morak.simone@gmail.com

DOI: 10.1175/JCLI-D-11-00678.1

(see also Kunkel et al. 2006; Pan et al. 2004; Meehl et al. 2012).

Changes in temperature extremes are not only influenced by external forcings. They can also be affected by changes in global circulation patterns, such as the North Atlantic Oscillation and the northern annular mode (Kenyon and Hegerl 2008; Scaife et al. 2008).

Detection studies aim to determine whether an observed change can be explained solely by internal climate variability or whether external factors also make a contribution. An observed change in climate is compared with the expected climate response to external forcings, which is estimated by climate models. The effect of the forcings is considered detectable if the observed change is significantly different (in a statistical sense) from internal climate variability.

Taking a step further, attribution analyses attempt to partition the observed change between possible causes, such as greenhouse gas emissions, volcanic aerosols, and so on (e.g., Hegerl et al. 1997; Tett et al. 1999; Stott 2003; Stott et al. 2010). Results have shown that observed changes in global and, in some regions, regional mean surface temperature since the mid-twentieth century can largely be attributed to an increase in greenhouse gases (see Hegerl et al. 2007).

There are notably fewer detection and attribution studies that examine recent changes in temperature extremes. Kiktev et al. (2003) were the first to apply detection attribution methods to extremes. They found that greenhouse gas emissions play a key role in the observed increase in warm minimum temperature extremes and decrease in cold minimum temperature extremes. Hegerl et al. (2004) carried out a model study on the detectability of changes in temperature and precipitation extremes and found that changes in extremes may be as detectable as changes in the mean.

Christidis et al. (2005) found detectable changes in the intensity of extremes—that is, the coldest and warmest daily minimum temperature of the year as well as the coldest daily maximum temperature. Recent studies by Christidis et al. (2011) and Zwiers et al. (2011) show a detectable increase in the outer tail of the distribution of warm daytime temperatures over the second half of the twentieth century. Morak et al. (2011) found significant changes in the frequency of warm nights on the global scale, especially in Northern Hemisphere regions. The study also found that large parts of the observed global scale trend in the frequency of warm nights are well predicted by the trend in mean temperature, which has been attributed largely to anthropogenic greenhouse gas increases, suggesting that the detected global-scale trend in the frequency of warm nights is at least partly anthropogenic.

The present study extends Morak et al. (2011) by examining changes in the warm and cold tails of the daily minimum and maximum temperature distribution during boreal cold [October–March (ONDJFM)] and warm [April–September (AMJJAS)] season separately. The work concentrates on changes from global and hemispheric scales to regional scales. It also examines the benefit of using an optimized detection methodology.

The paper is structured as follows: First, we describe the data and processing methods (section 2). We then compare the observed and model-simulated changes in the frequency of cold and warm extremes on global and regional scales (section 3). Our detection analysis is described in section 4. Results are presented in section 5, followed by a summary of the study and conclusions (section 6).

2. Data and processing

In this work, we compare observed and climate model-simulated trends in mean values of temperature extreme indices splitting the year into the dynamically active boreal cold (ONDJFM) and warm (AMJJAS) seasons [as used in studies by Meehl et al. (2004) and Cook et al. (2011)]. We define our indices relative to the 10th and 90th percentiles of the daily maximum and minimum temperatures during the base period 1961–90, which we use to compute threshold values. Index tn10 (frequency of cold nights) is defined as the percentage of days per month for which the daily minimum temperature does not reach the 10th percentile of the base period daily minimum, and tn90 (frequency of warm nights) represents the percentage of days where the daily minimum temperature exceeds the 90th percentile of the base period daily minimum. Similarly, tx10 (frequency of cold days) is defined as the percentage of days per month where the daily maximum temperature does not reach the 10th percentile of the base period daily maximum and tx90 (frequency of warm days) is the percentage of days where the daily maximum temperature exceeds the 90th percentile of the base period daily maximum. The indices have been computed separately for each grid box, using the gridbox-specific climatology. The advantage of using percentile indices, rather than absolute values, is that outliers do not have a strong impact on the index values, because an outlier only counts for one exceedance and does not introduce a bias through its actual magnitude or anomaly. The use of percentile indices also allows for comparison of changes across climatologically different regions (see Alexander et al. 2006).

This study uses one set of observed gridded indices as well as indices computed from daily minimum and maximum temperatures from climate model simulations

that have been driven with both natural and anthropogenic forcings. To determine variations in extremes stemming from internal climate variability, we also use data from a 1000-yr-long control run without forcings apart from the seasonal cycle (see below for more details).

First, the observational data are described. The observed gridded datasets of tn10, tn90, tx10, and tx90, which cover the period 1886–2005, were produced by binning the monthly values of the indices, computed from station data, into 5° × 5° grid boxes (see Morak et al. 2011). The index station data are the same as used by Kenyon and Hegerl (2008) and were produced as part of the Hadley Centre climate extremes (HadEX) project (Alexander et al. 2006). The values of each grid box are based on a varying number of observations and can therefore be noisy, especially if the value from a grid box represents just a small number of measurements. Unobserved regions remain blank; that is, no interpolation routine has been applied to fill them. A previous study (Morak et al. 2011) used this dataset and the HadEX dataset and found that the results were not sensitive to the observational data used. For this study, only data to 2003 are used since the spatial and temporal coverage drops substantially after 2003.

Next, we consider the model data. We use modeled daily minimum and maximum surface temperature data derived from simulations with the Hadley Centre Global Environmental Model, version 1 (HadGEM1), which has a grid resolution of 1.25° × 1.875°. HadGEM1 is the first of the HadGEM family of models, which have a nonhydrostatic dynamical core and employ a semi-implicit, semi-Lagrangian time integration scheme (Davies et al. 2005). Model simulations with HadGEM1 have been used in several detection and attribution analyses and also feature in the Fourth Assessment Report of the Intergovernmental Panel on Climate Change (IPCC AR4; Christidis et al. 2012; Hegerl et al. 2007). The equilibrium climate sensitivity of HadGEM1 is 4.4 K (Stott et al. 2006). These model data come from an ensemble of four twentieth-century simulations and a 1000-yr-long control run without any forcings (Martin et al. 2006; Stott et al. 2006). The twentieth-century simulations include both natural and anthropogenic drivers, such as time-varying volcanic aerosol and solar forcing, as well as changes in greenhouse gas concentrations, land use, anthropogenic aerosols, and black carbon. We use data from the experiment for the period 1950–2005. The control simulation does not include any forcing apart from the seasonal cycle. From the 1000 years of available daily data, we extracted 32 overlapping segments, each which are 53 years long. When performing the optimized analysis, these are split into one set of 16 chunks used to prewhiten the data and another to determine the uncertainty caused by internal variability.

The percentile indices are computed using the daily maximum and minimum temperature data using the FORTRAN code provided by the Expert Team on Climate Change Detection and Indices (ETCCDI; Klein Tank and Können 2003; Zhang et al. 2005; Alexander et al. 2006). This computation produces monthly values of tn10, tx10, tn90, and tx90 indices from each of the four runs with all forcings, as well as the control experiment. A bootstrap method (Zhang et al. 2005) is employed to avoid inhomogeneities between the climatological base period and the subsequent and precedent time.

After the index computation, the model datasets are regridded onto a 5° × 5° grid to compare with observations. All the model datasets, including the control simulation segments, are masked in space and time to reflect the data coverage of the observations. In all figures, results based on the boreal cold season are labeled "wi" and results for the boreal warm season are labeled "su." To investigate the temporal change in the frequency of extremes, the regional mean time series of all indices, estimated with both observations and data from the model runs, and averaged over the Northern and Southern Hemispheres, are plotted in Figs. 1 and 2, and are discussed below.

For the next part of the analysis, spatial trend patterns expressed as trend per decade for each index are computed separately for the boreal cold (winter half-years 1950/51–2002/03) and boreal warm season (summer half-years 1951–2003), from both observations and climate model simulations.

The linear trend for each 5° × 5° grid box is computed by fitting a slope line using a least squares fit and is expressed as percent per decade. The linear trend is only computed for grid boxes where at least five years of data are available during the first and last decade of the analysis period. These linear trend patterns are shown in Figs. 3–6 (discussed in detail below) for cold and warm extremes in winter and summer. Linear least squares trend patterns are often used in detection and attribution analyses that focus on determining causes of large-scale changes (e.g., Hegerl et al. 1997, 2004; Zhang et al. 2007) and generally capture recent changes well. Although Figs. 1 and 2 suggest that the trend would be stronger when focusing on a more recent period, the longer analysis period improves the signal-to-noise ratio by being less affected by internal climate variability [Morak et al. (2011) for tn90].

To reduce the amount of spatial noise and to focus on spatial scales larger than the gridpoint scale, a five-point smoother is applied to all datasets by computing the average of each grid box and its adjacent four grid boxes

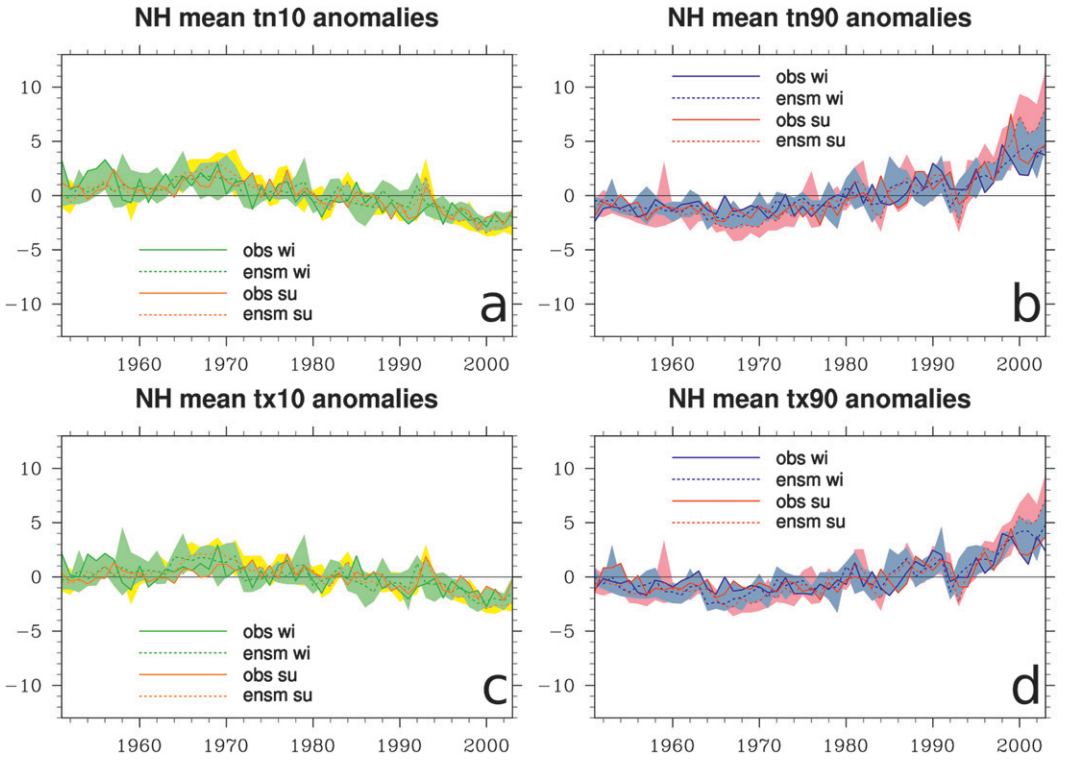

FIG. 1. Northern Hemisphere mean change (anomalies relative to the average from 1951 to 2003 and expressed as percentage change in the frequency of days) in the frequency of (a) cold nights (tn10), (b) warm nights (tn90), (c) cold days (tx10), and (d) warm days (tx90). Solid lines show observed anomalies, dashed lines represent the ensemble mean anomalies, and shaded areas show the ensemble spread. Changes in cold extremes (tn10 and tx10) during the boreal cold season (ONDJFM) are shown in green (light green shading) and those during the boreal warm season (AMJJAS) are shown in orange (yellow shading). Changes in warm extremes (tn90 and tx90) during the boreal cold season are displayed in blue (gray-blue shading) and those during the boreal warm season in red (light pink shading).

prior to plotting and the detection analysis. To illustrate whether the trend patterns of the individual ensemble members are represented well by the ensemble mean, grid boxes where all four runs have the same sign are stippled in Figs. 3c,d–6c,d, described below. This is a simple nonparametric test of where the simulated trend pattern is robust relative to internal climate variability.

The detection analysis encompasses a range of spatial scales (global, hemispheric, and regional; see Table 1). Regions that are bigger than the more frequently used Giorgi regions (Giorgi and Francisco 2000) are used, in order to increase the signal-to-noise ratio and to adjust the analysis to data availability. However, our regions encompass many of the smaller Giorgi regions.

3. Observed and model-simulated changes in frequency of extremes

The time series of Northern and Southern Hemispheric land average frequency in cold days and nights (see Figs. 1a,c and 2a,c) show a decrease for both observations and model simulations that started in the 1970s and lasted until the end of the analysis period. The observed changes, expressed in percentage change in the frequency of days, correspond to a decrease of approximately 5–6 days over the analysis period. In the Northern Hemisphere, the decrease in the number of cold nights (tn10; Fig. 1a) is slightly larger than the decrease in the number of cold days (tx10; Fig. 1c) for both the boreal cold season (green lines and light green shading) and boreal warm season (orange lines and yellow shading). The changes in tx10 during the boreal warm season are smaller than the ones during the boreal cold season (Fig. 1c). The Southern Hemispheric mean time series (Figs. 2a,c) displays higher variability than the Northern Hemisphere equivalent, probably because of fewer land areas and poorer data coverage in the Southern Hemisphere.

Hemispherically averaged time series of the number of warm days and nights (tn90 and tx90) (Figs. 1b,d) show an increase since the 1970s. The observed changes, expressed in percentage change in the frequency of days,

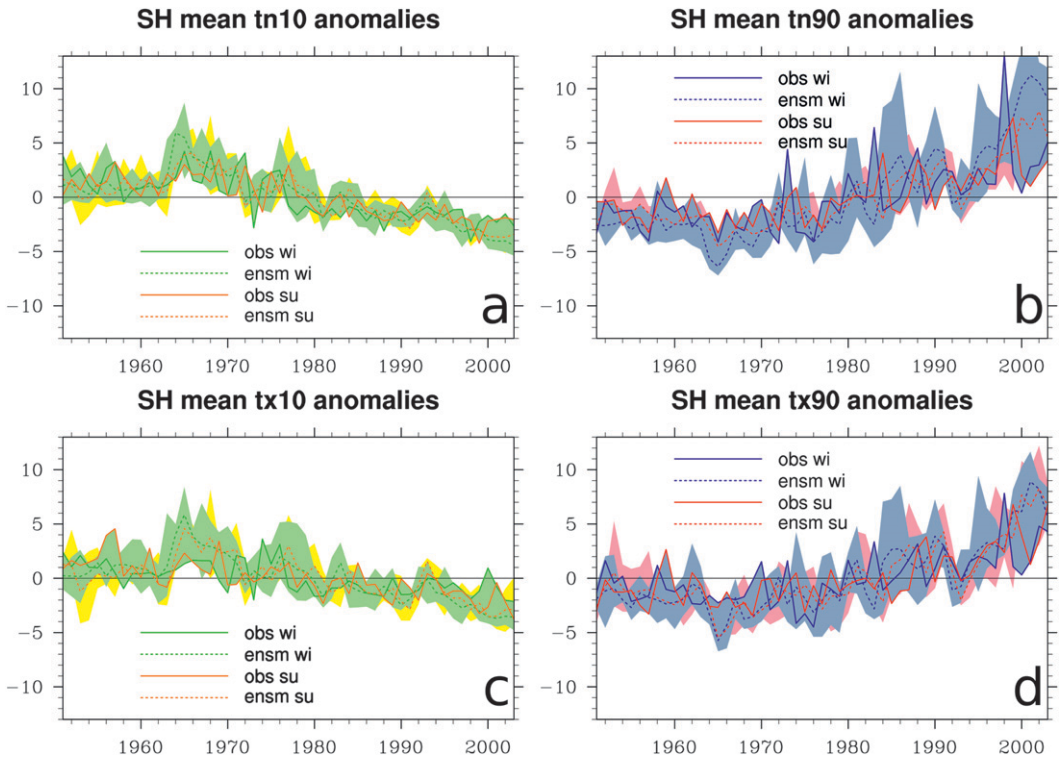

FIG. 2. As in Fig. 1, but for the Southern Hemisphere.

correspond to an increase of approximately 7–9 days over the analysis period. In the Northern Hemisphere, the warm nights index (Fig. 1b) shows a larger change than the number of warm days (Fig. 1d) during the boreal warm season. Changes in Northern Hemispheric tn90 and tx90 during the boreal cold season are smaller in magnitude than those during the boreal warm season (see blue lines and gray-blue shading in Figs. 1b,d).

Note that tn90 and tx90 display much larger fluctuations in the Southern Hemisphere for both model and data (Figs. 2b,d). Observed changes in Southern Hemisphere tn90 during the austral warm season (boreal cold season) and austral cold season (boreal warm season) have a similar magnitude to changes in the Northern Hemisphere (cf. Figs. 2b and 1b). However, observed changes in tx90 during the austral warm and cold season (boreal cold and warm season) across the Southern Hemisphere are larger than those of the Northern Hemisphere (cf. Figs. 2d and 1d).

We now turn to an analysis of the spatial pattern of change in extremes. The observed and simulated spatial trend pattern in the number of cold nights (tn10) during the boreal cold season (Figs. 3a,c) shows an overall decrease that is evident in most parts of the world. The strongest decrease is observed across central and Southeast Asia, and parts of northern Asia (see Fig. 3a). On the other hand, there are some grid boxes across the northeast coast of the United States and South America where a weak increase is observed (see Fig. 3a), even in regions where the model shows consistent (stippled) decreases. The model-simulated ensemble mean trend pattern shows a large-scale decrease of cold spells that are similar to those observed in many regions (Fig. 3c). However, the model does not reproduce the very strong observed decrease over parts of Asia. (see Figs. 3a,c).

The observed tn10 trend during the boreal warm season (Fig. 3b) shows smaller changes than during the

TABLE 1. Table of regions used in this study. Columns 1–3 number, list the acronyms, and give the names of the 10 regions. Columns 4 and 5 give the latitudinal and longitudinal extent of each region.

No.	Acronym	Name of region	Lat	Lon
1	GLOB	Global	All	All
2	NH	Northern Hemisphere	0°–90°N	All
3	SH	Southern Hemisphere	90°S–0°	All
4	EU	Europe	35°–75°N	10°W–40°E
5	SAS	Southern Asia	10°–45°N	40°E–180°
6	NAS	Northern Asia	45°–80°N	10°E–180°
7	AUS	Australia + New Zealand	60°–10°S	100°E/180°
8	WNA	Western North America	25°–55°N	135°–100°W
9	ENA	Eastern North America	25°–55°N	100°–45°W
10	NNAM	Northern North America	55°–75°N	165°–45°W

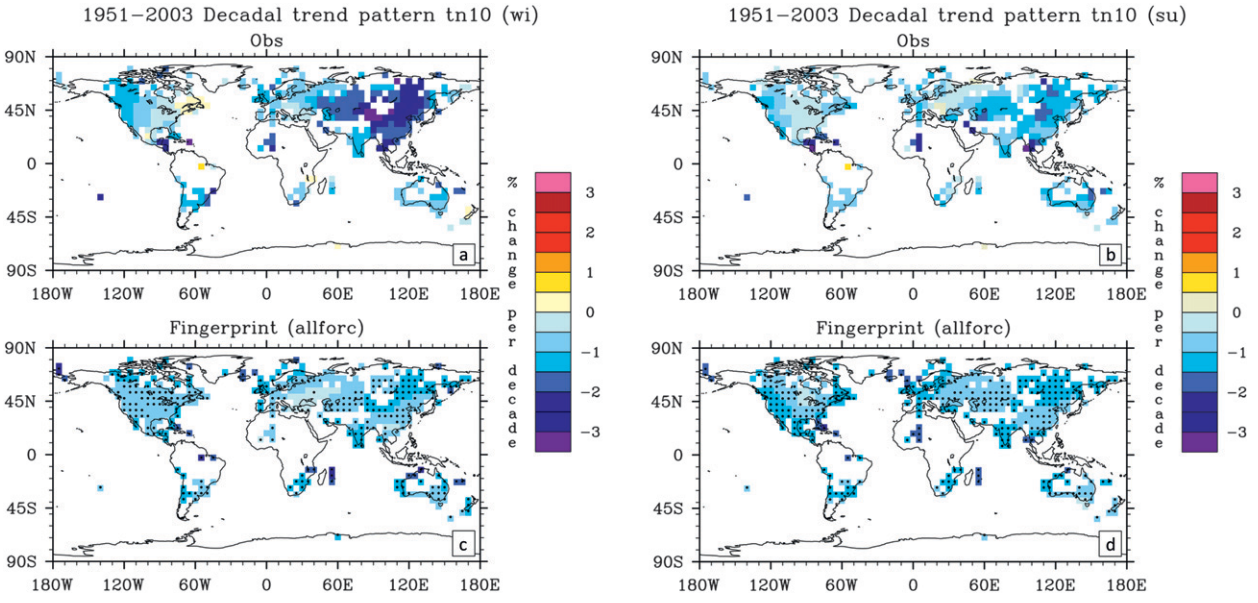

FIG. 3. Spatial trend pattern (in percent per decade) over the period 1951–2003 in the frequency in cold nights (tn10) during boreal (a) cold and (b) warm seasons for observations and (c) cold and (d) warm seasons for the ensemble mean. The stipples superimposed on the ensemble mean trend pattern mark the grid boxes where all four ensemble members agree in the sign of their trend. Spatial trend patterns have been smoothed by a 5-point spatial smoother (see body of paper) to focus on large-scale features.

boreal cold season (Fig. 3a). The largest observed decreases are found across most parts of Asia, while very little decrease is observed across eastern Europe (Fig. 3b). The simulated trends also indicate a large scale decrease in the frequency of cold nights.

The observed trend pattern for the frequency of cold days (tx10) in boreal winter (Figs. 4a,c) also shows a general decrease in the number of cold days, with some pronounced regional exceptions, such as in eastern North America, where a slight increase in the number of cold days is observed. Similar to the winter changes in tn10, the strongest observed decrease occurs over parts of Asia. The model-simulated trend pattern shows an overall decrease, which is robust across ensemble members (stippled) even in some regions where the observations show a weak increase. Changes in both observed

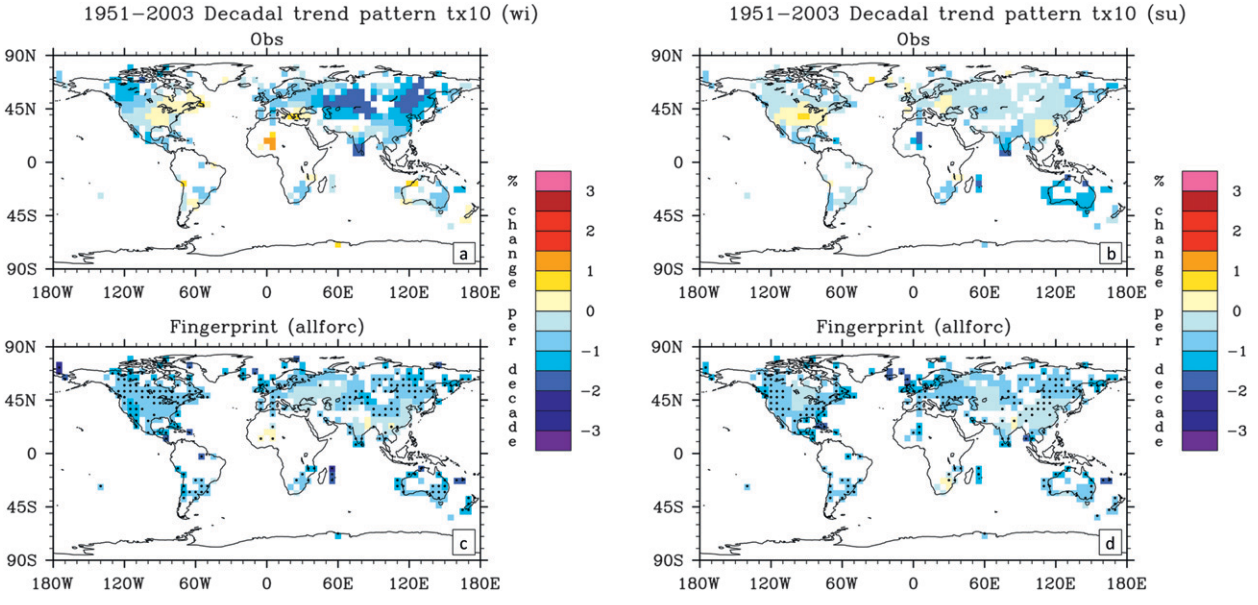

FIG. 4. As in Fig. 3, but for the change in the frequency in cold days (tx10).

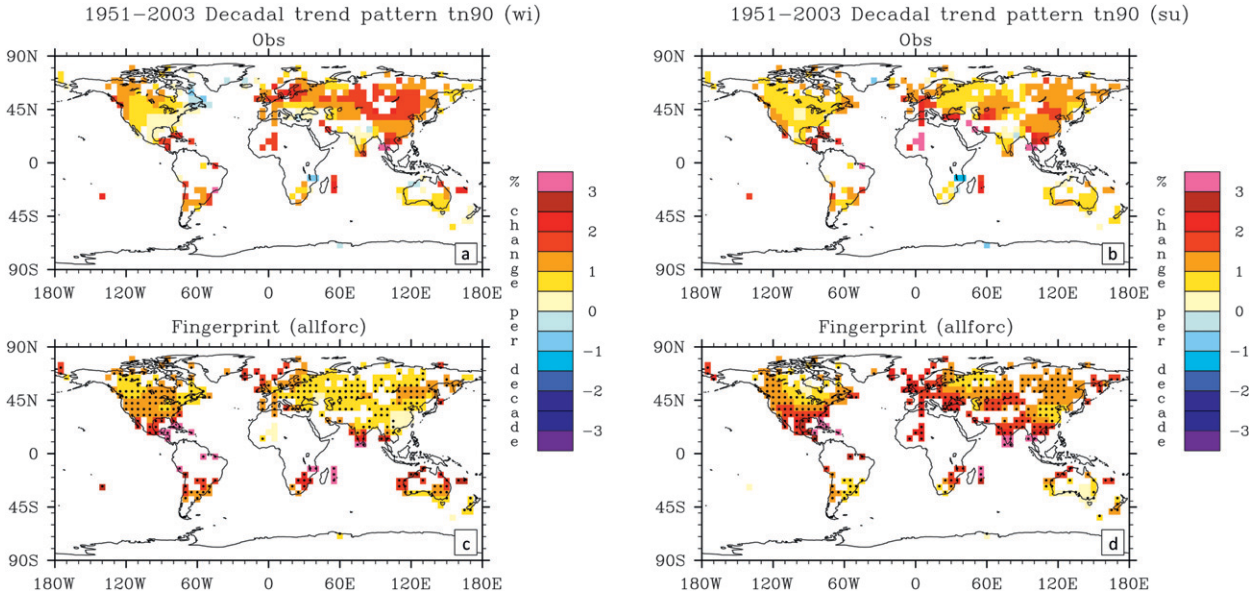

FIG. 5. As in Fig. 3, but for the change in the frequency in warm nights (tn90).

and model-simulated tx10 (see Figs. 4a,c) are generally of lower magnitude than those of tn10 (see Figs. 3a,c).

The observed trend pattern for the number of cold days (tx10) during the boreal warm season shows a small decrease across most parts of the world (Figs. 4b,d). As for the cold season, there are a few regions showing changes of the opposite sign, such as large parts of eastern North America (where in some points the model, in contrast, shows robust decreases across all four ensemble members), southeastern Asia, and parts of eastern Europe. The simulated ensemble mean pattern shows larger trends than observations over many regions and does not feature any increases (see Fig. 4d).

The frequency of warm nights and warm days shows a general increase in models and observations (Figs. 5 and 6). The observed trend pattern of number of warm nights (tn90) during the boreal cold season shows an overall increase across most parts of the world (Figs. 5a, c), which is strongest in central Asia, northern Europe, and over many tropical grid points. This enhancement of

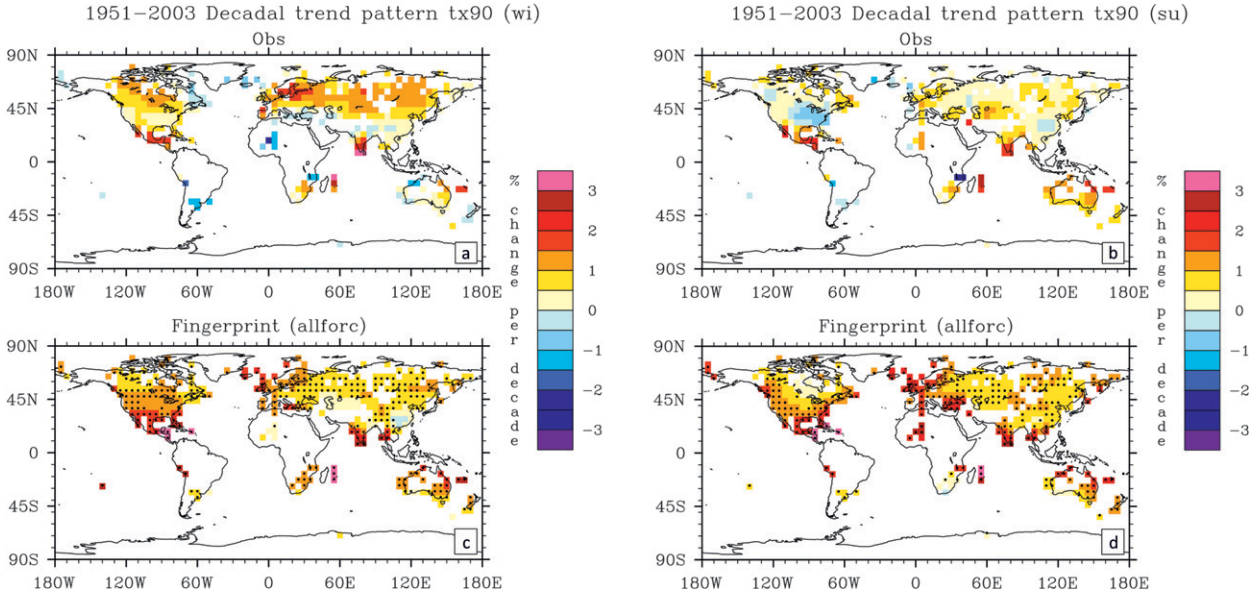

FIG. 6. As in Fig. 3, but for the change in the frequency in warm days (tx90).

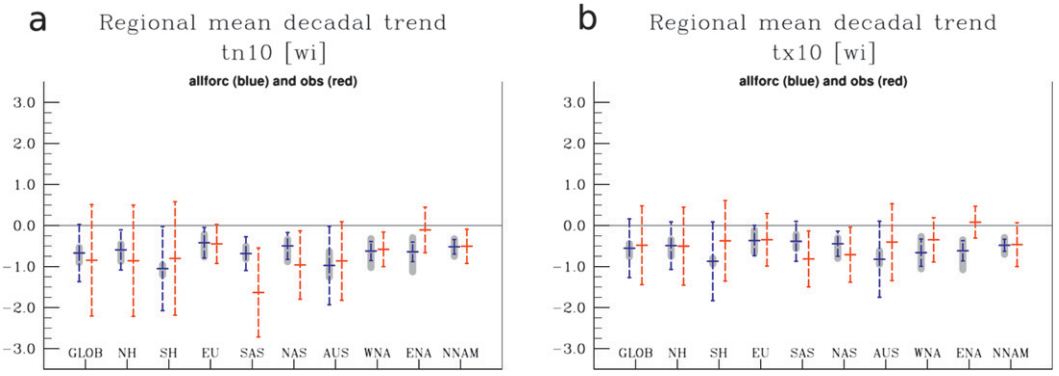

FIG. 7. The (a) tn10 and (b) tx10 regional mean decadal trend for the boreal cold season (horizontal line marker) and spread of two standard deviations computed across all grid boxes in the region, representing the spatial variability (vertical line; percent per decade). Red symbols represent the observed values and blue ones those of the all-forced ensemble. The gray shading in the background of the blue symbols represents the range of the regional mean trend values spanned by the four ensemble members.

trends in the tropics was also observed in Morak et al. (2011) and is probably due to smaller climate variability in the tropics, leading to a tn90 threshold that is easier to exceed with warming in both models and observations. Smaller changes, and even a small area of slight decrease, are observed in many parts of eastern North America (see Fig. 5a). The model manages to reproduce the overall increase in tn90, with changes that are robust across ensemble members over most grid points. However, the model does not reproduce the strong increase over Asia in winter.

Figures 5b,d shows the observed and simulated trend pattern of tn90 during the boreal warm season. In some areas where the observed trend (Fig. 5b) is smaller than during the boreal cold season (Fig. 5a), the model indicates larger trends (cf. Fig. 5d with Fig. 5c).

The trend pattern of the frequency of warm days (tx90) during the boreal cold season also indicates a widespread increase (see Fig. 6a,c). However, this increase is smaller than the increase in tn90 (see Fig. 5a). Trend values of small magnitude are observed in the United States and Southeast Asia, some of which are reproduced by the model. The simulated changes in the frequency of warm days are larger at low latitudes (see Fig. 6c) and are larger than the observed ones in parts of North America. Observed trends in parts of western Australia in the austral summer are much smaller and are even regionally negative in the observations.

The observed trend (see Fig. 6b) in the tx90 index during the boreal warm season is smaller than that observed during the boreal cold season (see Fig. 6a), with significant areas of decrease in the frequency of hot days, including parts of North America and Asia. The ensemble mean from the model does not reproduce these regional decreases, and instead shows robust increases over some of the same regions (see Fig. 6d).

Figures 7 and 8 illustrate the regionally averaged trends of the changes in the frequency of extremes (taking into account the varying gridbox size) and their variability across grid boxes from observations (red symbols) and simulations (blue) for boreal winter. The figures also show the spread (maximum minus minimum) of the regional mean trend (gray bar) of the individual ensemble

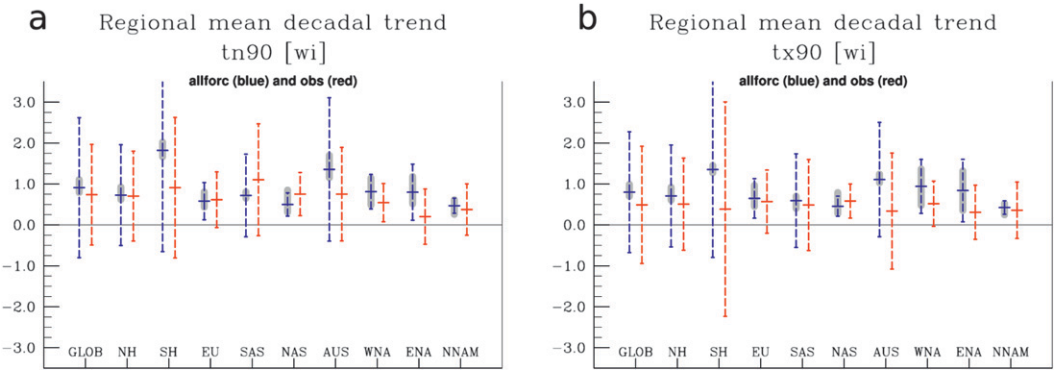

FIG. 8. As in Fig. 7, but for the (a) tn90 and (b) tx90 regional mean decadal trend for the boreal cold season.

members to illustrate the extent to which the regionally averaged trends vary across individual simulations. The figures show that the spatial variability of tn10 and tx10 (Fig. 7) is smaller in comparison with to tn90 and tx90 (Fig. 8). We also find that in western and eastern North America, Europe, and northern Asia, there is a large variation of the regional mean trend values within the ensemble. The observed area mean trend is within the model range for many but not all regions.

4. Detection analysis

To determine whether the observed trend is significantly larger than expected from variability generated within the climate system, and whether it is consistent with the fingerprint of forced changes plus variability, an optimal detection analysis has been applied. The fingerprints are derived from the ensemble mean of simulations with all forcings. Two sets of 16 segments, extracted from the control run are used to provide estimates of the internal climate variability and to carry out the prewhitening process (see below).

The fingerprint analysis is based on a total least squares regression and aims to explain the observed changes as a linear combination of changes caused by anthropogenic and natural forcings as well as changes caused by internal variability [see Allen and Stott (2003) for a detailed mathematical description of this analysis]:

$$\mathbf{Y} = (\mathbf{X} - \boldsymbol{\nu})\alpha + \text{res}. \quad (1)$$

Here $\mathbf{Y}$ represents the vector of the observations (Y_1, . . . , Y_i), where Y_i denotes the observed gridbox trend values of the index for the boreal cold or warm season. Also, $\mathbf{X}$ is the model fingerprint vector (X_1, . . . , X_i), comprising model estimates of the gridbox trend values computed from the ensemble mean of the model simulations with all forcings; and $\boldsymbol{\nu}$ stands for the model internal variability and is estimated from the control segments (the fingerprint is averaged from four simulations and the noise variance is hence reduced by a factor of 4). Finally, α is the scaling factor that determines the magnitude of the fingerprint in observations; res is the regression residual and is assumed to be due to internal climate variability.

The scaling factor α is the factor by which the fingerprint has to be scaled in order to best match the observations. The uncertainty in α has been computed by adding noise onto both the fingerprint and the observations and repeating the scaling factor calculations (Allen and Stott 2003).

In the optimized analysis, all data are first prewhitened using the inverse covariance matrix of climate variability (see Allen and Tett 1999). To be able to invert the covariance matrix, all data are projected onto the space of the first few empirical orthogonal functions (EOFs) of control run variability, thus reducing the spatial dimension of the covariance matrix (Hegerl et al. 1997; Allen and Tett 1999). The regression equation is the same as Eq. (1), although the regression is now computed on prewhitened data expressed in the space of the truncated eigenvectors rather than grid points (Allen and Tett 1999).

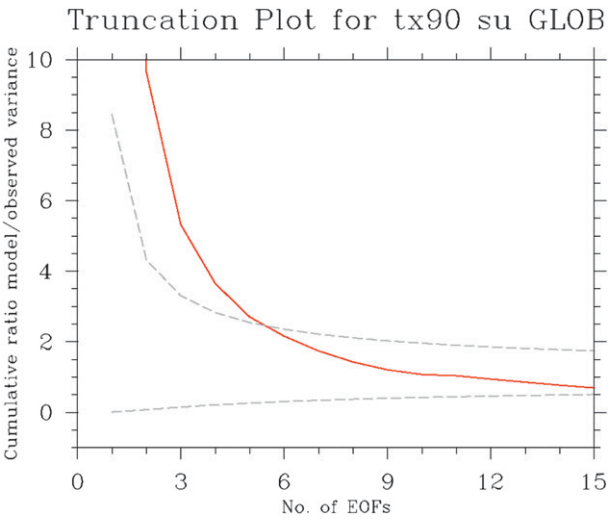

FIG. 9. The change of the ratio of the cumulative model and observed residual variance with truncation for the global decadal trend in tx90 during boreal warm season for each truncation level between 2 and 15 in the optimal fingerprint analysis (solid red line). Also shown are the upper and lower limits of the 5–95% range for the chi-squared test (dashed gray lines).

An important step is to determine the level of truncation that sufficiently represents the spatial fingerprint trend patterns, excluding EOFs that do not add any further information, or which reflect small-scale variability that is not well reproduced in model simulations. The truncation level is determined by analyzing the regression residual (res) in a chi-square test (Allen and Tett 1999), ensuring that the observed variance lies within the 5%–95% range of the model variability. In the best case, the ratio of the modeled and observed variance is close to unity of the chosen truncation level. Figure 9 illustrates the results of the chi-squared test for the global trend in tx90 during the boreal warm season and indicates that a truncation level of about 12 is adequate. Different truncation levels are chosen for each spatial region, and where no truncation level yields residuals consistent with model variability, this indicates that either the model variability in the chosen region is inappropriate or the observed variability contribution is unusually high or that the fingerprint does not sufficiently capture the observed trend pattern (e.g., because of model deficiencies or missing forcings).

The scaling factors α are computed for all indices, all regions, and both half-year trends using both the nonoptimized and optimized approach. Following this, the residuals of the regression are calculated and are tested to determine if they are consistent with the model estimates of internal variability. Regions where the variability is significantly larger than simulated are excluded from the analysis.

If the fifth percentile of the scaling factor is greater than zero, the observed climate change is said to be detectable. We consider a change detected if it is detectable at least for the optimal analysis, as that is expected to be more powerful. In cases where the regression residual is only consistent with model variability in the nonoptimized case, this may be due to a strong loss of spatial fingerprint information as a result of truncation. Hence we consider the few cases where this occurs, such as for warm austral winter days in the Australian region (see below), as successful despite being based on the nonoptimal analysis.

5. Results of the detection analysis

In this section, we present results of the detection analysis for all indices and investigate potential benefits from the optimized approach. Changes are detectable when they are significantly different from those driven by internal variability alone. A scaling factor of 1 implies that the ensemble mean trend perfectly represents the observed trend and, therefore, it does not need to be scaled, and a scaling factor consistent with 1 given uncertainty indicates that the model is statistically consistent with the observations.

a. Detectability of trends in cold extremes

Figures 10a and 10b show results from the optimized (solid) and nonoptimized (dashed) fingerprint analyses of the trend in tn10 during the boreal cold and warm seasons, respectively. The results for the boreal cold season (see Fig. 10a) show a high detectability, with the exception of the SAS region for which the regression residual is not consistent with noise using either of the analysis methods. We also find that optimizing leads to a larger number of detectable regions, while in the nonoptimized spatial trend analysis several regions show regression residual variability that is not consistent with that in the model control simulation. This may be due to the larger spatial variability across data points than resolved in the model, a problem that is avoided by truncating to a small number of spatial EOFs in the optimized analysis.

During the boreal warm season (see Fig. 10b), all 10 regions show a trend that is found to be significantly different from changes solely attributable to internal variability, when using a nonoptimized analysis. Here, 8 of 10 regions show detectable changes when an optimized analysis is used. Changes in tn10 during the boreal warm season show the largest detectability, with all regions containing significant changes that are generally consistent with the model-simulated changes (scaling factor ranges encompassing 1). In the boreal winter analysis only northern Asia (which has very large observed trends) yields regression residuals that are not consistent with climate model variability.

Changes in tx10 during the boreal cold season (see Fig. 10e) are detectable in a larger number of regions in the optimized analysis (9 out of 10) compared with the nonoptimized one (6 out of 10). The only region that does not show significant changes using either approach is Europe.

Changes in the tx10 index during the boreal warm season (see Fig. 10f) are found to be detectable in 7 out of 10 regions using an optimized analysis and in 6 out of 10 for the nonoptimized. No detectable changes are found in Europe and eastern North America. Optimization leads to a slight improvement of the number of regions with detectable signals (see Fig. 10f).

Overall, the model-simulated trend pattern expected in response to external forcing is detected in the observed change in the global frequency of cold daytime and nighttime extremes. Changes are also detected in the Northern and Southern Hemispheres and across most regions (over Europe for the frequency of cold winter and summer nights; for southern Asia for all indices except the frequency of cold winter nights; for eastern North America for all but the frequency of cold summer days; and for northern Asia, Australia and New Zealand, western North America, and northern North America for all indices in the cold tail). Using an optimized analysis improves the number of detectable regions for all cold extreme indices, except the changes in the frequency of cold summer nights.

b. Detectability of trends in warm extremes

Figures 10c and 10d show results from the optimized and nonoptimized detection analyses of the trend in tn90 during the boreal cold season and the boreal warm season, respectively. We find detectable changes during the boreal cold season in 8 out of 10 regions with optimization and in 5 out of 10 regions without optimizing. The Southern Hemisphere is the only region where no detectable change is found using either approach, since the regression residual is again not consistent with noise.

The fingerprint analysis of the trend in frequency of warm nights in the boreal warm season suggests a slightly lower number of detectable regions for the optimized analysis compared to the boreal cold season. The optimized analysis indicates detection in 7 out of 10 regions

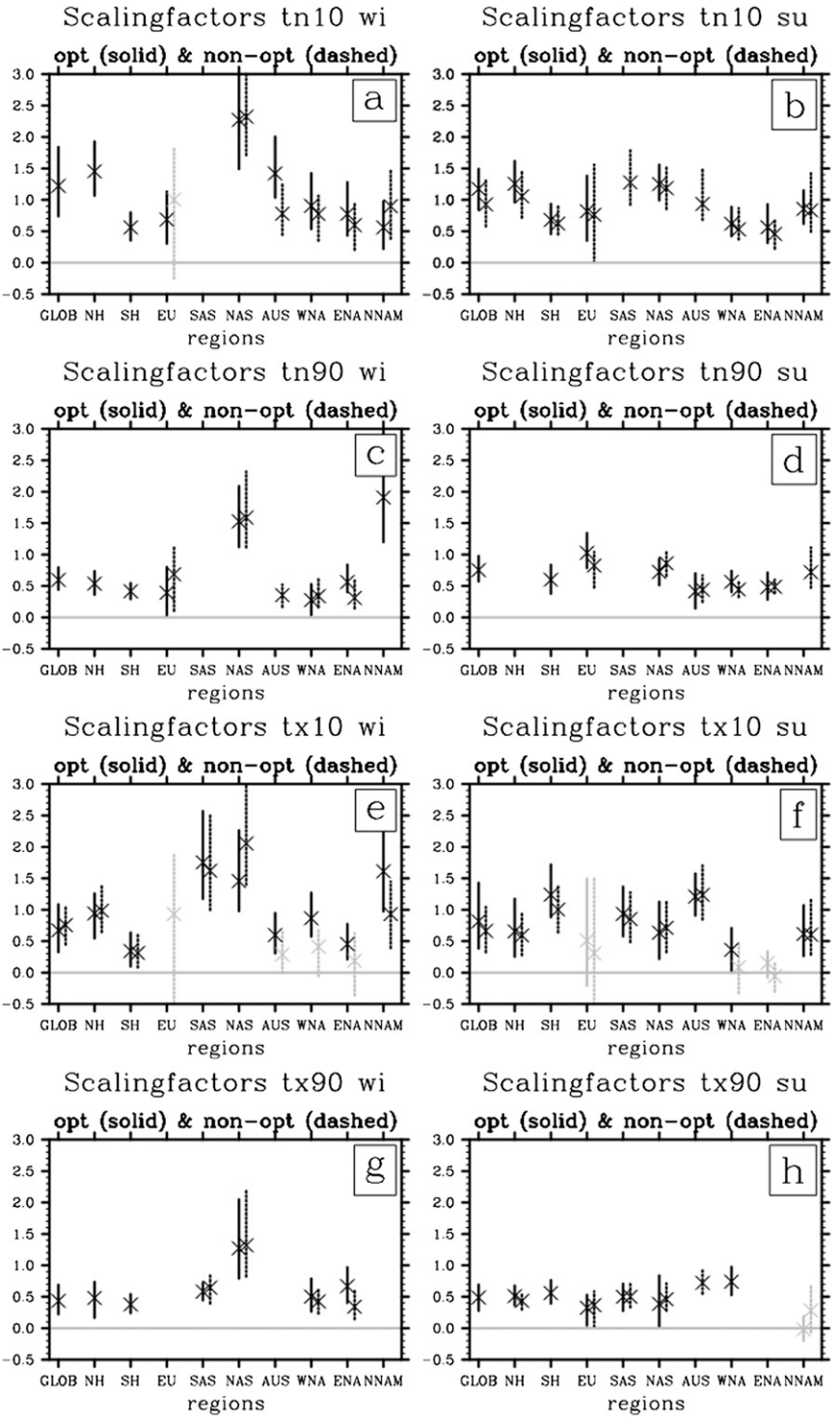

FIG. 10. Scaling factors [Eq. (1)] by which the model mean fingerprint has to be scaled to reproduce the observed trend, plus its 5%–95% uncertainty range for (a) tn10 during boreal cold season, (b) tn10 during boreal warm season, (c) tn90 during boreal cold season, (d) tn90 during boreal warm season, (e) tx10 during boreal cold season, (f) tx10 during boreal warm season, (g) tx90 during boreal cold season, and (h) tx90 during boreal warm season. Black lines and symbols denote detectable regions; gray lines and symbols stand for those not detectable. Missing symbols indicate regions for which the regression residual is statistically inconsistent (at the 5% level) with the model estimate of internal variability.

and the nonoptimized analysis shows detectable changes in 6 out of 10 regions. Global and Southern Hemispheric changes are detectable only when using the optimized method, whereas significant changes and consistent residuals across northern North America are only found in the nonoptimized analysis. Thus, overall, all regions, except for the Northern Hemispheric and the southern Asian regions, show detectable changes, with the regression residual being problematic for the Northern Hemisphere as a whole and southern Asia, even when optimizing, and for several regions in the nonoptimized analysis.

The detection analysis of the trend in tx90 during the boreal cold season (see Fig. 10g) shows detectability in 7 out of 10 regions for the optimized analysis and in 4 out of 10 regions for the nonoptimized analysis. Europe is the only region not showing significant changes in either analysis, a result of the residual being inconsistent with model variability.

Figure 10h shows the results of the tx90 analysis during the boreal warm season and indicates detectability in 7 out of 10 regions for the optimal and in 5 out of 10 regions for the nonoptimized approach. Global and Southern Hemispheric changes as well as changes in western North America are only detectable using an optimal approach. Changes in northern North America are not outside the range of internal climate variability.

In summary, the model-simulated trend pattern expected in response to external forcing is detected in the observed change in the global, Northern Hemispheric (in all indices except for warm summer nights), and Southern Hemispheric frequency of warm day and nighttime extremes. Detectable changes have also been observed for all indices in Europe (except warm winter days), southern Asia (only for changes in warm winter and summer days), northern Asia (where winter changes are significantly larger than in the model), Australia and New Zealand, eastern North America (for all indices except changes in warm summer days), and western and northern North America (only for changes in warm winter and summer nights). Changes in the frequency of hot summer days and warm winter days are significantly larger in the model than observed in almost all regions, particularly so in the summer.

Optimizing improves the results of the detection analysis for the changes in the frequency warm extremes.

6. Discussion and conclusions

This study shows that the observed decrease in the number of cold extremes (tn10 and tx10) and increase in the number of warm extremes (tn90 and tx90) during boreal cold and warm seasons are generally well reproduced by model simulations with HadGEM1 forced using both natural and anthropogenic drivers. The highest number of regions with detectable changes corresponds to the tn10 index and its change during the boreal warm season.

The model significantly underestimates changes in some regions, particularly in winter across large parts of Asia (scaling factors not consistent with 1), and has a tendency to overestimate changes in the frequency of hot days in both the winter and summer seasons over most regions, and in the global and hemispheric mean. It also overestimates changes in the frequency of warm winter days on larger scales, which may be due to either too large a forcing or model response over that period. The model reproduces changes in cold extremes within the uncertainty range on large scales, but does underestimate them in some regions. Despite the observed overall decrease in tn10 and tx10 and increase in tn90 and tx90, there are some regions with trends of the opposite sign, such as changes in tx90 and tx10 during the boreal warm season, tx90 during the austral warm season in western Australia, and tx10 during the boreal cold season across large parts of eastern North America.

The particular regional trend pattern, often also referred to as the ''warming hole,'' is not evident in the simulated trend pattern (Kunkel et al. 2006; Pan et al. 2004; Portmann et al. 2009; Meehl et al. 2012). Portmann et al. (2009) speculate that the warming hole could be related to changes in land use in the region, which would affect the concentration of biogenic aerosol and the hydrological cycle. Other possible explanations include regional-scale circulation effects, such as cold-air advection during winter and moisture convergence at low levels during summer (Meehl et al. 2012, unpublished manuscript).

In contrast, the observed changes indicate stronger warming (a decrease in cold extremes; an increase in warm extremes) over large parts of Eurasia in the boreal cold season. The change is most pronounced in the number of cold nights, where it extends far into eastern Asia, but also occurs in the frequency of warm nights, and least in the frequency of warm days. The strong changes in Eurasia may be caused by changes in circulation, particularly the upward trend of the northern annular mode over much of the late twentieth century (Thompson et al. 2000), which will lead to changes in all temperature extremes indices over Asia in the cold season (Kenyon and Hegerl 2008). This is consistent with Figs. 3–6 and probably leads to the very large scaling factors found for northern Asia (Fig. 10). In contrast, the strong trends in southern Asia in cold winter night anomalies prevent detection, as the regression residual is inconsistent with model estimates. This suggests that the change there is spatially more complex than can be

addressed by inflating the model-simulated change, pointing at regional circulation changes or forcings.

The detection analysis indicates a clear benefit from using an optimized approach, with the exception of the changes in the frequency of cold summer nights. Optimizing particularly improves the detectability for global and hemispheric changes in the number of cold nights, and warm days and nights during the boreal cold season and in warm days and nights during the boreal warm season. In some regions, particularly those with changes that are different from expectation, the analysis yields inconsistent residuals and with it no detection. Examples are southern Asia for winter minima and eastern North America for summer maxima.

In conclusion, we find that there is a significant increase in the trend in warm temperature extremes and a decrease in cold extremes during both boreal cold and warm season over the second half of twentieth century, which is detectable on the 5% confidence level globally and over many regions. We have not attempted to attribute these changes to a combination of forcings by applying a multifingerprint approach (Hegerl et al. 1997; Tett et al. 1999). Morak et al. 2011 showed that change in the frequency of warm nights corresponds well to changes in annual mean temperatures, even on temporal scales not affected by the trend, suggesting that detectable changes in warm nights are at least partially due to greenhouse gas increases. The changes detected in the frequency of warm nights and days, and hot days, are also consistent with the expectation from the observed change in mean temperature. This suggests that greenhouse gas forcing has contributed to the observed changes. However, only an attribution analysis can determine the magnitude of the greenhouse gas contribution to the changes detected in the frequency of temperature extremes.

Acknowledgments. Many thanks are given to Peter Stott, Helen Hanlon, and Darren Slevin for their support and suggestions and to three reviewers for their constructive and perceptive comments that helped improve the manuscript. The gridded dataset used has been produced by Jesse Kenyon. This study has been supported by the Centre for Earth System Dynamics (CESD), the Edinburgh Compute and Data Facility (ECDF), NFS Grant ATM-0296007, the U.S. Department of Energy's Office of Science and Office of Biological and Environmental Research, the National Oceanic and Atmospheric Administration's Climate Program Office (IDAG group), and NERC (NEH0035331). Nikolaos Christidis was supported by the Joint DECC/Defra Met Office Hadley Centre Climate Programme (GA01101).

REFERENCES

Alexander, L. V., and Coauthors, 2006: Global observed changes in daily climate extremes of temperature and precipitation. *J. Geophys. Res.,* **111,** D05109, doi:10.1029/2005JD006290.

Allen, M. R., and S. F. B. Tett, 1999: Checking for model consistency in optimal fingerprinting. *Climate Dyn.,* **15,** 419–434, doi:10.1007/s003820050291.

——, and P. A. Stott, 2003: Estimating signal amplitudes in optimal fingerprinting. Part I: Theory. *Climate Dyn.,* **21,** 477–491, doi:10.1007/s00382-003-0313-9.

Brown, S. J., J. Caesar, and C. A. T. Ferro, 2008: Global changes in extreme daily temperature since 1950. *J. Geophys. Res.,* **113,** D05115, doi:10.1029/2006JD008091.

Caesar, J., L. Alexander, and R. Vose, 2006: Large-scale changes in observed daily maximum and minimum temperatures: Creation and analysis of a new gridded data set. *J. Geophys. Res.,* **111,** D05101, doi:10.1029/2005JD006280.

Christidis, N., P. A. Stott, S. Brown, G. C. Hegerl, and J. Caesar, 2005: Detection of changes in temperature extremes during the second half of the 20th century. *Geophys. Res. Lett.,* **32,** L20716, doi:10.1029/2005GL023885.

——, ——, and ——, 2011: The role of human activity in the recent warming of extremely warm daytime temperatures. *J. Climate,* **24,** 1922–1930.

——, ——, F. Zwiers, H. Shiogama, and T. Nozawa, 2012: The contribution of anthropogenic forcings to regional changes in temperature during the last decade. *Climate Dyn.,* **39,** 1259–1274, doi:10.1007/s00382-011-1184-0.

Cook, B., R. Seager, and R. Miller, 2011: Atmospheric circulation anomalies during two persistent North American droughts: 1932–1939 and 1948–1957. *Climate Dyn.,* **36,** 2339–2355, doi:10.1007/s00382-010-0807-1.

Davies, T., M. J. P. Cullen, A. J. Malcolm, M. H. Mawson, A. Staniforth, A. A. White, and N. Wood, 2005: A new dynamical core for the Met Office's global and regional modelling of the atmosphere. *Quart. J. Roy. Meteor. Soc.,* **131,** 1759–1782, doi:10.1256/qj.04.101.

Frich, P., L. V. Alexander, P. Della-Marta, B. Gleason, M. Haylock, A. M. G. Klein Tank, and T. Peterson, 2002: Observed coherent changes in climatic extremes during the second half of the twentieth century. *Climate Res.,* **19,** 193–212, doi:10.3354/cr019193.

Giorgi, F., and R. Francisco, 2000: Evaluating uncertainties in the prediction of regional climate change. *Geophys. Res. Lett.,* **27,** 1295–1298, doi:10.1029/1999GL011016.

Hegerl, G. C., K. Hasselmann, U. Cubasch, J. F. B. Mitchell, E. Roeckner, R. Voss, and J. Waszkewitz, 1997: Multi-fingerprint detection and attribution analysis of greenhouse gas, greenhouse gas-plus-aerosol and solar forced climate change. *Climate Dyn.,* **13,** 613–634, doi:10.1007/s003820050186.

——, F. W. Zwiers, P. A. Stott, and V. V. Kharin, 2004: Detectability of anthropogenic changes in annual temperature and precipitation extremes. *J. Climate,* **17,** 3683–3700.

——, and Coauthors, 2007: Understanding and attributing climate change. *Climate Change 2007: The Physical Science Basis,* S. Solomon et al., Eds., Cambridge University Press, 663–745.

Karl, T., G. A. Meehl, C. D. Miller, S. J. Hassol, A. M. Waple, and W. L. Murray, 2008: Weather and climate extremes in a changing climate—Regions of focus: North America, Hawaii, Caribbean, and U.S. Pacific islands. NOAA NCDC, 164 pp.

Kenyon, J., and G. Hegerl, 2008: Influence of modes of climate variability on global temperature extremes. *J. Climate,* **21,** 3872–3889.

Kharin, V. V., and F. W. Zwiers, 2000: Changes in the extremes in an ensemble of transient climate simulations with a coupled atmosphere–ocean GCM. *J. Climate,* **13,** 3760–3788.

——, ——, X. Zhang, and G. C. Hegerl, 2007: Changes in temperature and precipitation extremes in the IPCC ensemble of global coupled model simulations. *J. Climate,* **20,** 1419–1444.

Kiktev, D., D. M. H. Sexton, L. Alexander, and C. K. Folland, 2003: Comparison of modeled and observed trends in indices of daily climate extremes. *J. Climate,* **16,** 3560–3571.

Klein Tank, A. M. G., and G. P. Können, 2003: Trends in indices of daily temperature and precipitation extremes in Europe, 1946–99. *J. Climate,* **16,** 3665–3680.

Kunkel, K. E., X.-Z. Liang, J. Zhu, and Y. Lin, 2006: Can CGCMs simulate the twentieth-century ''warming hole'' in the central United States? *J. Climate,* **19,** 4137–4153.

Martin, G. M., M. A. Ringer, V. D. Pope, A. Jones, C. Dearden, and T. J. Hinton, 2006: The physical properties of the atmosphere in the new Hadley Centre Global Environmental Model (HadGEM1). Part I: Model description and global climatology. *J. Climate,* **19,** 1274–1301.

Meehl, G. A., W. M. Washington, C. M. Ammann, J. M. Arblaster, T. M. L. Wigley, and C. Tebaldi, 2004: Combinations of natural and anthropogenic forcings in twentieth-century climate. *J. Climate,* **17,** 3721–3727.

——, J. M. Arblaster, and G. Branstator, 2012: Mechanisms contributing to the warming hole and the consequent U.S. east–west differential of heat extremes. *J. Climate,* **25,** 6394–6408.

Morak, S., G. C. Hegerl, and J. Kenyon, 2011: Detectable regional changes in the number of warm nights. *Geophys. Res. Lett.,* **38,** L17703, doi:10.1029/2011GL048531.

Pan, Z., R. W. Arritt, E. S. Takle, J. W. Gutowski, C. J. Anderson, and M. Segal, 2004: Altered hydrologic feedback in a warming climate introduces a warming hole. *Geophys. Res. Lett.,* **31,** L17109, doi:10.1029/2004GL020528.

Portmann, R. W., S. Solomon, and G. C. Hegerl, 2009: Spatial and seasonal patterns in climate change, temperatures, and precipitation across the United States. *Proc. Nat. Acad. Sci.,* **106,** 7324–7329.

Scaife, A. A., C. K. Folland, L. V. Alexander, A. Moberg, and J. R. Knight, 2008: European climate extremes and the North Atlantic oscillation. *J. Climate,* **21,** 72–83.

Solomon, S., D. Qin, M. Manning, M. Marquis, K. Averyt, M. M. B. Tignor, H. L. Miller Jr., and Z. Chen, Eds., 2007: *Climate Change 2007: The Physical Science Basis.* Cambridge University Press, 996 pp.

Stott, P. A., 2003: Attribution of regional-scale temperature changes to anthropogenic and natural causes. *Geophys. Res. Lett.,* **30,** 1728, doi:10.1029/2003GL017324.

——, G. S. Jones, J. A. Lowe, P. Thorne, C. Durman, T. C. Johns, and J.-C. Thelen, 2006: Transient climate simulations with the HadGEM1 climate model: Causes of past warming and future climate change. *J. Climate,* **19,** 2763–2782.

——, N. P. Gillett, G. C. Hegerl, D. J. Karoly, D. Stone, X. Zhang, and F. Zwiers, 2010: Detection and attribution of climate change: A regional perspective. *WIREs Climate Change,* **1,** 192–211, doi:10.1002/wcc.34.

Tebaldi, C., K. Hayhoe, J. M. Arblaster, and G. A. Meehl, 2006: Going to the extremes: An intercomparison of model-simulated historical and future changes in extreme events. *Climate Change,* **79,** 185–211.

Tett, S. F. B., P. A. Stott, M. R. Allen, W. J. Ingram, and J. F. B. Mitchell, 1999: Causes of twentieth-century temperature change near the earth's surface. *Nature,* **399,** 569–572, doi:10.1038/21164.

Thompson, D. W. J., J. M. Wallace, and G. C. Hegerl, 2000: Annular modes in the extratropical circulation. Part II: Trends. *J. Climate,* **13,** 1018–1036.

Trenberth, K., and Coauthors, 2007: Observations: Surface and atmospheric climate change. *Climate Change 2007: The Physical Science Basis,* S. Solomon et al., Eds., Cambridge University Press, 235–336.

Vose, R., and Coauthors, 2005: Maximum and minimum temperature trends for the globe: An update through 2004. *Geophys. Res. Lett.,* **32,** L23822, doi:10.1029/2005GL024379.

Zhang, X., G. Hegerl, F. Zwiers, and J. Kenyon, 2005: Avoiding inhomogeneity in percentile-based indices of temperature extremes. *J. Climate,* **18,** 1641–1651.

——, F. W. Zwiers, G. C. Hegerl, F. H. Lambert, N. P. Gillett, S. Solomon, P. A. Stott, and T. Nozawa, 2007: Detection of human influence on twentieth-century precipitation trends. *Nature,* **448,** 461–465, doi:10.1038/nature06025.

Zwiers, F. W., X. Zhang, and Y. Feng, 2011: Anthropogenic influence on long return period daily temperature extremes at regional scales. *J. Climate,* **24,** 881–892.